Fundamental limitations for imaging GEO satellites

D. Mozurkewich

Seabrook Engineering, Seabrook, MD 20706 USA

H. R. Schmitt, J. T. Armstrong

Naval Research Laboratory, Washington, DC 20375 USA

We investigate the issue of whether an optical interferometer with baselines long enough to resolve details of a geostationary satellite can be phase stabilized. We conclude that it is possible to phase such an interferometer with shorter baselines using the techniques of baseline and wavelength bootstrapping, and that these shorter baselines are not so short as to make the instrument impractical. We conclude by showing the trade-off between the number of telescopes needed to phase the longest desired baselines and the diameter of those telescopes.

1. INTRODUCTION

Imaging a geosynchronous satellite from the ground is difficult. Reaching a resolution of $x = 10$ cm to yield 100 resolution elements across a 10 m target at a distance of $R = 37,500$ km requires an adaptive-optics-corrected telescope of diameter $D = R\lambda/x \approx 187$ m if it is observing at a wavelength $\lambda = 0.5\,\mu$m.

Building a telescope that large is impractical, if not currently impossible, but this resolution – 10 cm at geosynchronous altitude corresponds to 2.7 nanoradians or 0.55 mas (milliarcseconds) – can be reached with optical interferometry, as astronomical interferometers have demonstrated. A simple two-element interferometer consists of two telescopes separated by a baseline **B**. This baseline samples the Fourier transform of the target image at the spatial frequency $B_\perp/\lambda$, where $B_\perp$ is the component of **B** perpendicular to **s**, the unit vector pointing toward the center of the target. When the beams from the two telescopes are combined, they produce interference fringes (either spatially or temporally, depending on the type of beam combiner use), with the fringe visibility represented by $V = |V|\exp(i\phi)$. We measure V at as many spatial frequencies as practical, by using baselines of different lengths and/or orientations, and/or by using different wavelengths, and then Fourier transform the data to form an image.

The fringe amplitude, $|V|$, depends on the size scale(s) in the target image and on the resolution, λ/B, of the baseline. $|V| = 1$ corresponds to a target that is small compared to λ/B, but on the long, high-resolution baselines that will reveal target structure, $|V|$ becomes small. The signal-to-noise ratio SNR $= \sqrt{nV^2/2}$ in a data frame with n photons, so it also drops on these long baselines. In order to reach a given SNR, we need, for example, 10^4 times as many photons when $|V| = 0.01$ as when $|V| = 1$.

The fringe phase, ϕ, depends on source structure and can vary with baseline length and orientation, since different baselines are responsive to different size scales in the target. More important to the practicalities of operating the interferometer, atmospheric turbulence causes phase fluctuations ϕ_{atm} typically much larger than those due to source structure, and does so on atmospheric coherence timescales, t_0, of a few milliseconds.

The combination of low $|V|$ on the high-resolution baselines and large ϕ_{atm} means that we cannot detect the fringes within an atmospheric coherence time, so we cannot integrate to build up the SNR. However, we can work around this limitation by using a chain of telescopes. For example, if we use a line of N equally-spaced telescopes in which each of the $N - 1$ shortest baselines has high enough SNR for us to detect the fringe within t_0, we can determine the phase changes on the long (i.e., high spatial frequency) baseline by summing the phase changes on the short (low spatial frequency) baselines. This technique is known as *baseline bootstrapping*. We can also employ *wavelength bootstrapping*: use the fringe phase at a long wavelength, where we are observing at a low spatial frequency, to determine the phase at a shorter wavelength, i.e., a higher spatial frequency.

Send correspondence to David Mozurkewich, Seabrook Engineering, 9310 Dubarry Ave., Seabrook MD 20706
E-mail: dave@mozurkewich.com

Thus we need an array of multiple telescopes to keep the interferometer – and the long baselines in particular – in phase. Clearly, the size, D, of the individual telescopes and the number, N, of telescopes needed to make the baseline chain must be traded against one another to produce an interferometer with the desired resolution and sensitivity. In this paper, we work through the sensitivity and phase transfer error issues to produce a relationship between D and N.

Section 2 presents our assumptions about the instrument design, target brightness and photometric throughput. In Section 3 we describe the fringe visibilities and photon fluxes that the geosatellite imaging problem presents to us. Section 4 describes the contributions of photon noise and atmospheric turbulence to the overall phase errors. In Section 5 we describe how we translate these error contributions into constraints on the diameter of the telescopes in the array in the case of a five-telescope circular array. Finally, in Section 6 we extend those results to the trade-off between telescope size and telescope number.

2. ASSUMPTIONS

The overall instrumental configuration that we assume is an interferometer that uses both baseline bootstrapping and wavelength bootstrapping, with telescopes equipped with adaptive optics. Our configuration tracks fringes at near-infrared wavelengths, but that does its imaging at visible wavelengths in order to keep the baselines short. We consider both linear and circular configurations of N telescopes[1],[2]. The phase-tracking infrared beam combiner uses pairwise combination, as opposed to all-on-one combination.

Our array is located at a fairly good site with a Fried parameter $r_0 = 10$ cm and a wind speed $v_\mathrm{w} = 10\,\mathrm{m\,s^{-1}}$. We assume the current state of the art for data processing. If new techniques become available, for example a way to determine the atmospheric phase without detecting fringes, similar performance could be achieved with significantly smaller telescopes.

Since we are more interested in what should be possible rather than what is easy to build, we assume fairly aggressive requirements for the Strehl ratio of the adaptive optics system and for system throughput. We assume the wavefront has $\sigma_\mathrm{WF} = 0.122\,\mu$m error after the adaptive optics system. The Strehl ratio varies as $S = \exp[-(2\pi\sigma_\mathrm{WF}/\lambda)^2]$ giving $S = 0.4$ at $\lambda = 0.8\,\mu$m. We assume a total system throughput $T = 0.33$ (not including the Strehl ratio), based on assumptions for detector quantum efficiency ($Q = 0.7$), size of the telescopes' central obstruction (10% of light lost), coupling to a single-mode fiber (80% efficiency), and reflection losses (67% efficiency, based on 98% reflectivity at 20 surfaces in the optical train).

Both read noise and sky background will be negligible. In regard to read noise, we assume a 5 ms frame rate and 50 spectral channels in each of the two beam combiner outputs, which gives 20,000 reads per second. For a 1.5 meter telescope, read noise will equal photon noise when the read noise is 6 electrons rms in the infrared K band. HgCdTe avalanche photodiodes are currently about 1 electron rms across the entire near infrared. We can safely assume that by the time this instrument is built, performance will be limited by photon noise.

The comprehensive discussion of the background radiation sources affecting astronomical observations is Leinert et al. [3]. Converting to a consistent set of units, the sky brightness in K and H are both about magnitude 13.5 for a one square arc second field of view. The background decreases 2 to 3 magnitudes at J and another 5 magnitudes or more into the visible. Of necessity, these are approximate, varying with time and site, but are small enough they can be ignored in our present context.

Finally, in order to estimate the dependence of our results on these requirements, we repeat the analysis with one third the system throughput.

3. FRINGE VISIBILITY AND PHOTOMETRY

In order to model the detectability of the interference fringes for tracking on the short baselines and for taking data on the long baselines that characterize details of the target, we need to estimate the fringe SNR. Since the SNR is proportional to $|V|$ and $|V|$ decreases as the baseline length B increases, the magnitude of $|V|$ on the short baselines determines the number of telescopes needed to phase the array, while the magnitude of $|V|$ on the longest baseline determines how long we must integrate in order to generate an image.
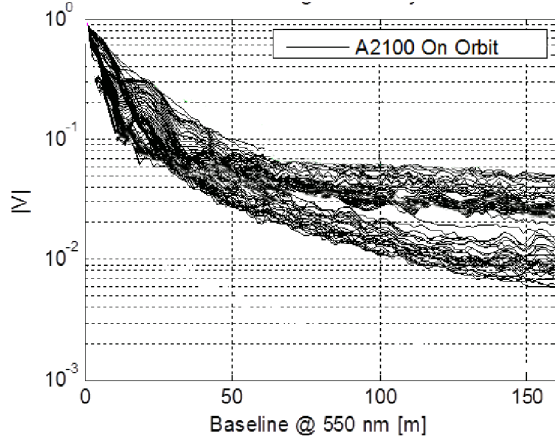
Figure 1 Simulated fringe visibility amplitudes as a function of baseline length at $\lambda = 0.550\,\mu\text{m}$ for a Lockheed-Martin A2100 bus. Each trace is the visibility for a different azimuth.
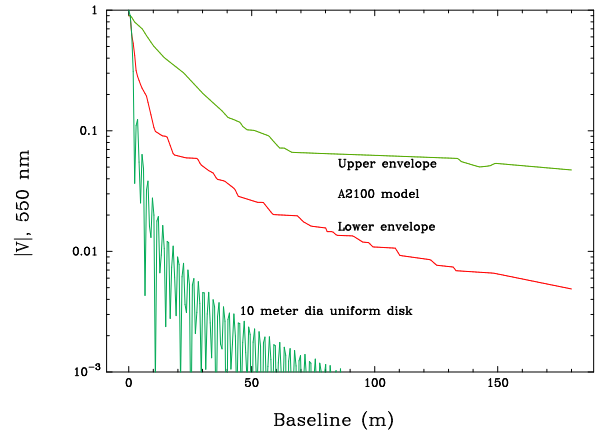

Figure 2 Envelopes of the A2100 model visibilities shown in Fig. 1 (upper two curves), and visibilities of a 10 m uniform disk (lower curve). In the text, the upper two curves are referred to as the high-$|V|$ and low-$|V|$ models.

In order to estimate the target fringe visibility, we used imaging simulations of an A2100 bus from the DARPA deep space imaging workshop. Figure 1 shows the visibilities for this model, observed on baselines out to 160 m at $\lambda = 0.55\,\mu\text{m}$. Each trace corresponds to a different azimuth. To simplify our analysis, we used the upper and lower envelopes of these visibilities, as shown in the upper two curves in Fig. 2. In the discussion below, we refer to these curves as the high-$|V|$ and low-$|V|$ models and assumed the target is gray; that is, the visibility at other wavelengths can be obtained by multiplying the baseline by the ratio of wavelengths.

The lower curve in Fig. 2 shows the visibilities of a uniformly-bright disk target 10 m in diameter. Even though the overall size scales of the uniform disk and the A2100 model are similar, the A2100 model shows much higher visibilities even on baselines as short as 10 m. The reason for this difference is that the only high spatial frequency in the uniform disk is due to its edge, while the A2100 has abundant high-spatial-frequency structure due to the details of its structure.

Some discussions of phasing long-baseline interferometers have implicitly assumed a uniform disk as the target, which produces a fringe visibility that drops steeply with baseline length. These discussions have concluded that the baseline length needed to produce a fringe visibility strong enough to track within t_0 is so short, and the resulting number of telescopes needed to produce the long baseline needed for high resolution is so large, that the accumulating phase errors along the chain of short baselines would make it impossible to keep the long baseline in phase. This figure demonstrates the importance of using a realistic target model in assessing the feasibility of interferometric imaging. Our discussion in this paper will show that phasing the long baselines is in fact practical.

The other variable that affects SNR is the number of photons, n, in the data frame. The photometric signal is given by

$$n = F_0(\lambda)\,10^{-0.4m_\lambda}\left(\frac{\lambda}{hc}\right)\left(\frac{\pi D^2}{4}\right)TQS(\lambda)\,\Delta\lambda, \tag{1}$$

where $F_0(\lambda)$ is the zero-magnitude flux and m_λ is the magnitude of the target, both at a given wavelength λ. The total bandwidth is $\Delta\lambda$. For fringe tracking with a pairwise beam combiner, we assume we use half the light from each of the two telescopes for fringe tracking, so those factors of $1/2$ and 2 cancel. Using our assumed values for T and Q, a telescope diameter $D = 1.5$ m, and a 5 ms integration time, we calculate the photon rates for four wavelength regimes shown in Table 1. We used a target brightness in the visual V band () of $m_V = 11$. For typical geosats, which are more reflective at infrared wavelengths, this implies $m_{\lambda>1\mu\text{m}} = 8$. For each band,

Table 1. Photon rates per 5 ms for 1.5 m aperture

Band	$\lambda(\mu m)$	$\Delta\lambda(\mu m)$	$F_0(\lambda)^{\mathrm{a}}$	m_λ	$S(\lambda)$	n (5 ms)
V+R	0.70	0.40	1.835×10^{-8}	11.0	0.313	950
J	1.25	0.24	2.963×10^{-9}	8.0	0.695	5825
H	1.65	0.28	1.216×10^{-9}	8.0	0.812	4300
K	2.20	0.42	4.346×10^{-10}	8.0	0.889	3365

[a]0 magnitude flux in $\mathrm{W\,m^{-2}\,\mu m^{-1}}$

we calculated the Strehl ratio with

$$S(\lambda) = \exp\left[-(2\pi d_{\mathrm{WF}}/\lambda)^2\right],\tag{2}$$

choosing $d_{\mathrm{WF}} = 0.12\,\mu$m as indicated above.

4. INTEROMETRIC NOISE

Having laid out our assumptions and calculated photon rates, we now need to consider two sources of noise that will affect our phase measurements and hence our ability to phase the array. Photon noise limits performance for short averaging times, while motion of the fringe due to the atmosphere dominates for long averages. Instrumental effects on the phase can be measured and corrected, so we will neglect them here.

4.1. Phase error due to photon noise

Photon noise limits the accuracy to which we can measure the phase to no better than

$$\sigma_{\phi,\,\mathrm{phot}} = \left(\frac{2}{nt|V|^2}\right)^{1/2},\tag{3}$$

where n is the number of photons detected per unit time, t is the integration time and $|V|$ is the fringe amplitude. Since the phase is measured modulo 2π, this uncertainty is meaningless for signals smaller than $nt|V|^2/2 \approx 1$. To allow us to convert between wavelengths, we express this uncertainty in terms of delay (i.e., path differences between the two arms of the interferometer) via

$$\sigma_{d,\,\mathrm{phot}} = \left(\frac{\lambda}{2\pi}\right)\left(\frac{2}{nt|V|^2}\right)^{1/2}.\tag{4}$$

4.2. Phase error due to atmospheric fringe motion

The second source of noise is systematic motion of the fringe, which is dominated by density fluctuations along the line of sight due to the Earth's turbulent atmosphere. The expected difference between two phases at times separated by t is

$$\sigma_{\phi\,\mathrm{atm}}^2 = 2\left(\frac{t}{t_0}\right)^{5/3},\tag{5}$$

where $t_0 = 0.314 r_0/v$ is the atmospheric coherence time, r_0 is Fried's parameter and v is the wind speed. The coherence time is defined for a single line of sight through the atmosphere; the leading factor of two accounts for the interferometer measuring the phase difference between two paths. Normally, t_0 and r_0 are quoted for a wavelength of 0.5 μm; for other wavelengths, $\sigma_{\phi\,\mathrm{atm}}$ must be scaled by the ratio of the wavelengths. Of course, since the amplitude of the turbulence and the wind speed will vary along the line of sight, Eq. 5 uses an appropriately weighted wind speed.

In practice, the structure function overestimates the high-frequency components of the fringe motion since an aperture of diameter D reduces the power at frequencies higher than $\sim v/D$. This effect is shown in Fig. 3,
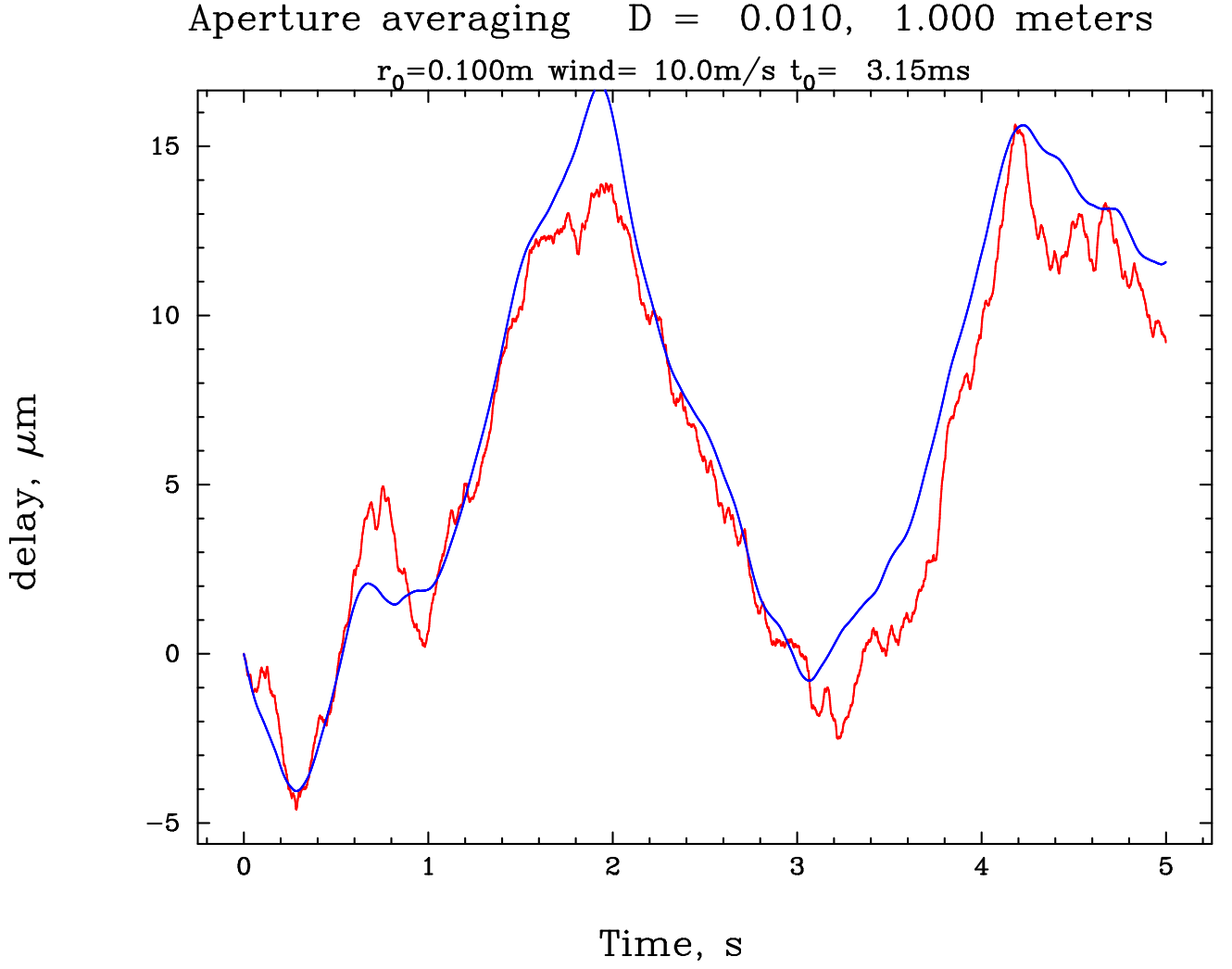
Figure 3 Fringe motion due to atmospheric turbulence for aperture diameters of 1 cm (red curve) and 1 m (blue curve). The data were generated with a simulated phase screen.

in which we show simulated delay variations due to a phase screen passing over a 1 cm aperture (red curve) and a 1 m aperture (blue curve). The delay measured by the larger aperture is missing all the high-frequency variations, but it is not just a smoothed version of the small-aperture delay. The larger aperture averages the phase screen in two dimensions. Since the phase screen is rarely symmetric perpendicular to the direction of the wind, the large-aperture phase can be systematically offset from that measured by the small aperture for significant periods of time.

Even though aperture averaging has a significant effect on the smoothness of the phase variations, the structure function, Eq. 5, is dominated by low-frequency variations so the effect of aperture averaging on averaging time is small. To take advantage of this smoothness, we need to adopt a Bayesian approach, using continuity and smoothness for priors, to search for a model which uses as few parameters as possible to give the delay with sufficient accuracy at all times.

There are several choices for the model; for this work, we use a purely heuristic approach and adopt a cubic spline to enforce continuity and smoothness. We keep the frame rates short enough to freeze the fringe motion: 2 to 4 ms for the visible and 5 to 10 ms for the infrared. Then we place a spline node every n^{th} frame and use maximum-likelihood estimation to determine the delay at each node by comparing the value of the spline for
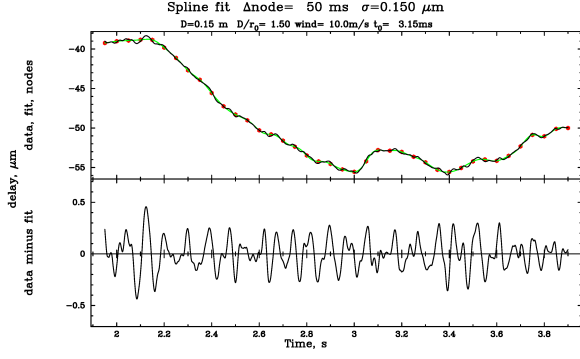
Figure 4 Model fitting of delay variations seen with a 15 cm diameter aperture. The simulated delays are shown in black in the upper panel. A cubic spline is fit to the data at the nodes, which are spaced by 50 ms (red). The resulting spline is shown in green (hidden by the data). The lower panel shows the residual between the data and the spline fit.
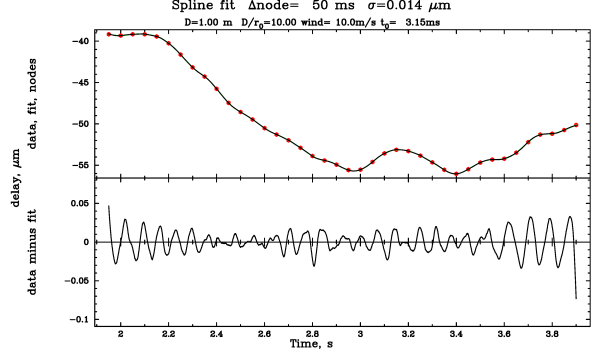
Figure 5 Model fitting of delay variations seen with a 1.0 m diameter aperture. Data, nodes, spline fit, and residuals are as in Fig. 4. Both figures were generated using the same phase screen but note that the fit to the larger aperture data is nearly an order of magnitude better than the fit to the small-aperture data even though both models have the same node spacing.

Table 2.   Parameters for power law fit to $\sigma_{d,\,\text{atm}}(\text{SNR})$

D (m)	A (nm)	b
0.50	53.5	0.85
1.00	43.6	0.85
1.50	37.5	0.81
2.00	35.6	0.81

each frame to the data. Examples of the results of applying this procedure to our simulated data are shown in Figs. 4 and 5 for a 15 cm aperture and a 1.0 m aperture, respectively. In both cases, we used node spacings of 50 ms. The fit to larger aperture data has significantly better performance.

We performed this procedure with varying values of fringe SNR (i.e., due to photon noise in a 5 ms frame) and with varying node spacings, from 5 ms to 5 s. The resulting rms of the residuals, $\sigma_{d,\,\text{atm}}$, is shown for a range of cases in Fig. 6. We see that across a wide range fringe SNR, the best-performing models have node spacings between 50 and 200 ms, where the contributions to the delay uncertainty from photon noise and unmodeled atmospheric phase fluctuations are roughly equal. From these results, we read the relationship between SNR and the minimum delay uncertainty. That relationship, displayed in Fig. 7, can be fit by a power law,

$$\sigma_{d,\,\text{atm}} = A(\lambda/\text{SNR})^b, \tag{6}$$

where the units of A are nm and the units of λ are μm. Finally, we repeated this procedure for different aperture sizes D, with the resulting power law parameters summarized in Table 2.

To complete the estimation of the atmospheric delay error, we proceed as follows:

1. For a specified baseline B and wavelength λ, read the visibility amplitude for either the high-$|V|$ or low-$|V|$ model from Fig. 2, adjusting the baseline length for the observing wavelength λ via $B(0.55\mu\text{m}/\lambda)$.

2. Read the count rate n from the last column of Table 1 and scale it to the appropriate telescope diameter.

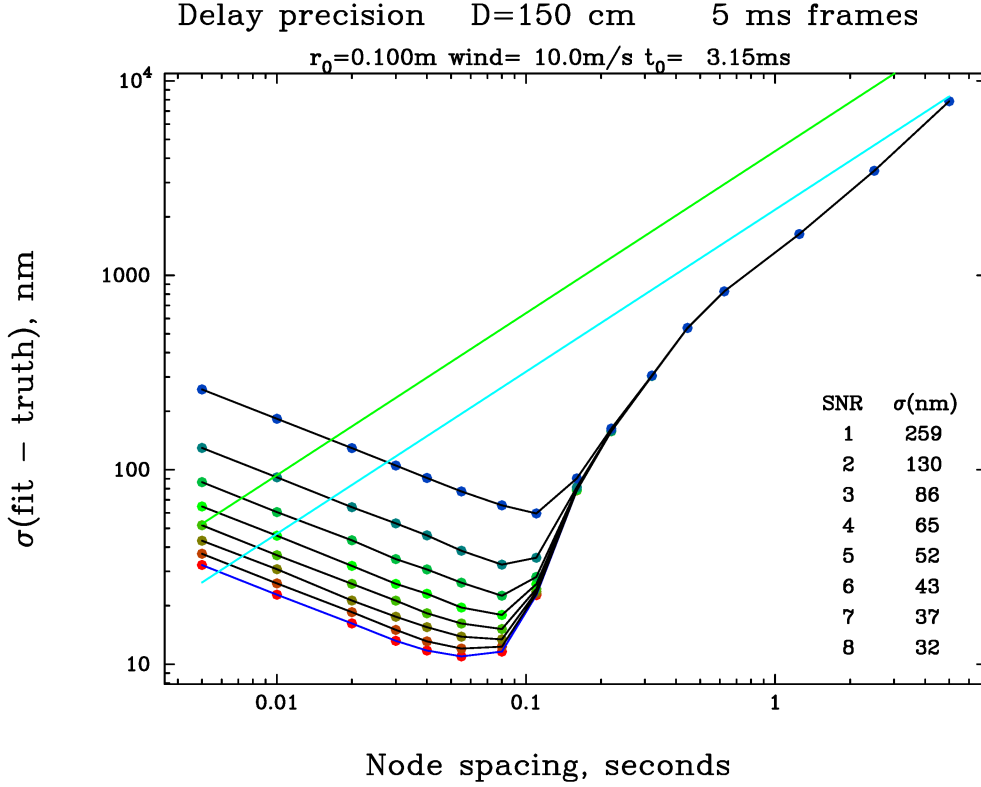3. Calculate the SNR with $\text{SNR} = \sqrt{n|V|^2/2}$.

Figure 6 The rms uncertainty, $\sigma_{d,\,\mathrm{atm}}$, in spline fits to atmospherically-induced delay variations as a function of spline node spacing, for various levels of fringe SNR. Each curve corresponds to a different value of the SNR in a 5 ms frame, with the lowest curve being for SNR = 8 ($\sigma_{d,\,\mathrm{phot}} = 32$ nm) and the highest for SNR = 1 (259 nm).

    4. Calculate the delay uncertainty $\sigma_{d,\,\mathrm{atm}}$ from Eq. 6 with the coefficients from Table 2.

    The results can be presented in different ways. In Fig. 8, the uncertainty is shown as a function of baseline length in each of the four spectral bands. This calculation used a pair of 1.5-meter diameter telescopes and the low-$|V|$ model. As expected, the visible band performs worst. In the infrared, the band with the highest count rates (J, the $1.13 - 1.37\,\mu$m band) performs the best: the higher visibility at longer wavelengths roughly compensates for the higher SNR required at those wavelengths to achieve the same delay precision.

    Fig. 9 compares performance for different telescope apertures.

5. PHASE-TRANSFER ERROR BUDGET

After measuring the phase on each of the short baselines at the fringe tracking wavelength, we need to transfer those phases to the long baselines at the imaging wavelength. In this section, we discuss the uncertainties in this procedure and give a simple error budget.

    During a coherent integration, the fringe is blurred by phase errors. We can write the fringe as

$$V = V_0 \exp(i\phi) \exp(i\epsilon), \tag{7}$$

where ϕ is the phase we want to measure and ϵ is the phase noise. Assuming that the phase error distribution is symmetric about zero, only variations in the component of V parallel to the fringe phasor $V_0 \exp(i\phi)$ will change $|V|$ and hence change the SNR. Thus, without loss of generality, we set $\phi = 0$, so the instantaneous value of $|V|$ is given by
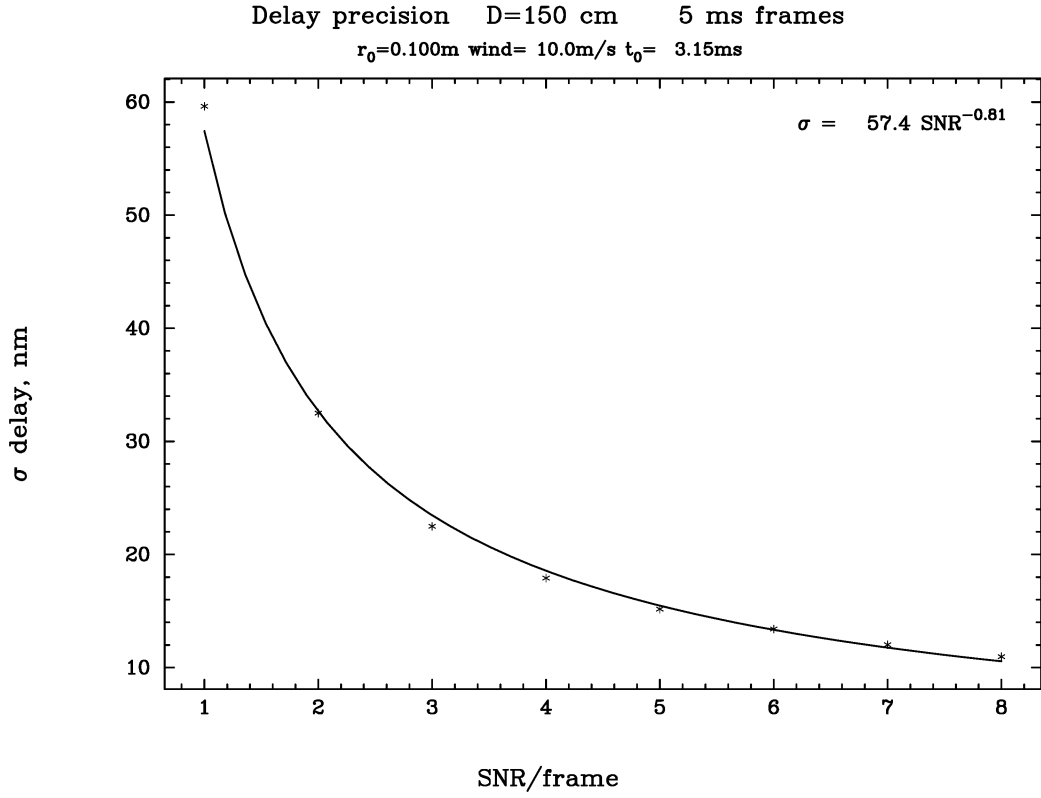
$$|V| = V_0 \cos(\epsilon). \tag{8}$$

Delay precision   D=150 cm   5 ms frames

r_0=0.100m wind= 10.0m/s t_0= 3.15ms

$\sigma =$ 57.4 SNR$^{-0.81}$

Figure 7 The variation of $\sigma_{d,\,\mathrm{atm}}$ with fringe SNR in the case of a 1.5 m aperture. The curve is a power law fit.

t= 0.010 s low SNR model

λ=1.65μm low−|V| model
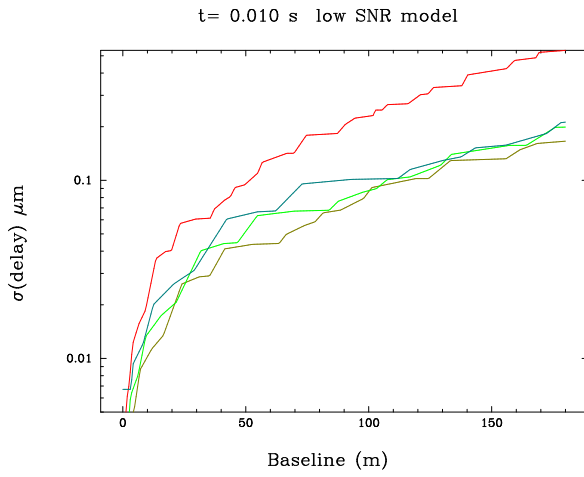
D = 0.50 m
D = 1.00 m
D = 1.50 m
D = 2.00 m

Figure 8 Single baseline delay uncertainty for a 1.5 m aperture, as a function of baseline length for the low-$|V|$ model. The four curves indicate the four spectral bands: red is visual (0.70 μm), orange is 1.25 μm, green is 1.65μm and blue is 2.20μm.
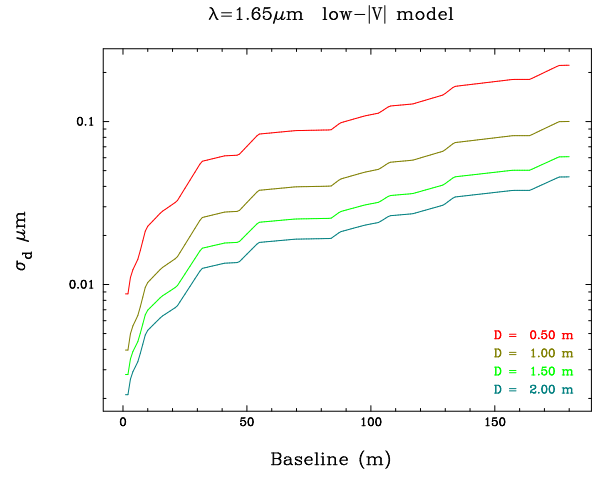
Figure 9 Single baseline delay uncertainty for the H spectral band, as a function of baseline length for the low-$|V|$ model. The four curves are for four aperture sizes ranging from 0.5 m (upper curve) to 2.0 m (lower curve).

Expanding the cosine and averaging over the error distribution gives

$$\langle |V| \rangle = V_0 \langle 1 - \frac{\epsilon^2}{2} \rangle = V_0 \left(1 - \frac{\sigma_\phi^2}{2} \right) = V_0 \exp(-\sigma_\phi^2/2). \tag{9}$$

For Gaussian noise, it is easy to show numerically that this approximation is good for σ_ϕ as large as 3. The time needed to achieve a specific SNR is proportional to $|V|^{-2} = \exp(\sigma_\phi^2)$.

Error propagation for baseline bootstrapping is relatively straightforward. For a linear array of N evenly-spaced telescopes, the phase estimate for the longest baseline is the sum of the phases on the $N-1$ short baselines and therefore, the phase uncertainty is just $\sqrt{(N-1)}\sigma_1$, where σ_1 is the phase error on the short baselines.

However, we can make a significant improvement in the phase estimate for the longest baseline if we use a ring of telescopes rather than a linear array. The long-baseline is half way around the ring; its phase is obtained by summing the phases on $N/2$ short baselines, but there are two independent ways to do the sum: clockwise and counterclockwise. The phase uncertainty is then $\sqrt{N/4}\,\sigma_1$. Of course, it takes approximately π times as many telescopes to reach the same maximum baseline length, but even so, the phase error on the longer baseline will be smaller for the circular array than for the linear array.

There is a second advantage to a ring configuration. With N telescopes in a line, there is only one pair of baselines with the largest separation; with a ring, there are $N/2$ longest baselines. Since most of the observation time is needed for the longest baselines, a ring configuration is significantly more efficient.

In addition to the phase errors from baseline bootstrapping, there are phase errors associated with wavelength bootstrapping. For wavelength bootstrapping, we assume that the fluctuation in phase on a baseline is due to a change in the density of the atmosphere along the line of sight. Thus to convert the measured phase at the fringe tracking wavelength to the phase at the imaging wavelength, we multiply by the ratio of refractivities for the two wavelengths. There are three sources of error in this calculation. Firstly, the index of refraction is uncertain due to an uncertainty in humidity. Secondly, for observations away from the zenith, different wavelengths follow different paths through to atmosphere due to differential refraction. Finally, we measure a weighted average of the phase over the aperture. The weighting depends on diffraction and thus on the wavelength.

So far, we have assumed the phase fluctuations are entirely due to the atmosphere. There will also be changes in path length through the optical system due to vibrations and thermal drift. Employing a metrology system will track these changes, but it will not be perfect; non-common-path errors will contribute at least a couple tens of nanometers to the delay uncertainty.

Finally, motion of the telescope parallel to the line of sight will contribute an error proportional to the index of refraction ($n \approx 1.0003$) rather than the refractivity ($n-1 \approx 1.01$). For a 5μm motion, this contributes 50 nm. We will need a metrology system to monitor the telescopes' positions during the observation.

Fortunately, all of the wavelength bootstrapping errors are station errors; they depend on the physics of what happens to a single beam propagating from the target through a telescope to the detector. The two telescopes at the ends of a bootstrapping chain contribute to the error budget but the interior telescopes do not since they contribute equally but with opposite signs to two baselines of which each one is a part.

Table 3 presents an error budget. For each item in the first part of the table, we show a delay error contribution in nanometers for a single baseline or telescope, a multiplier that characterizes how many such contributions from that item come into play, and the resulting contribution to the variance in nm^2 from that item. We then include the phase measurement error, translated into nanometers of delay error. The multiplier for this error contribution, $N/4$, corresponds to using a circular array.

Our final task is to see how the diameter of the single telescopes varies with N, the number of telescopes. We assume the telescopes are in a ring configuration. We start from the error budget in Table 3. A specified number of telescopes, N, determines both the length of the short baselines in that configuration and the phase uncertainty, $\sigma_d = 175/sqrtN$, that needs to be achieved on that baseline. Next, the relationships in Figure 9 are consulted to determine the phase uncertainty that can be achieved as a function of telescope diameter for that baseline. Finally that relationship is interpolated to determine the required telescope diameter.

Table 3.   Phase-transfer error budget

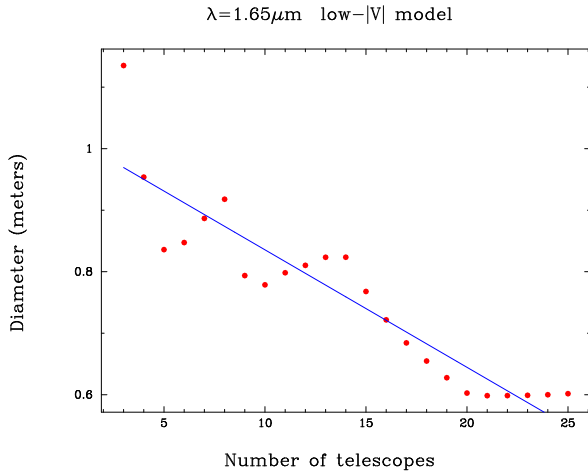| Item	Each σ(nm)	Multi-plier	Total σ^2 (nm)^2
Differential refraction	20	2	800
Aperture averaging	20	2	800
Humidity variations	15	1	225
Non-common-path errors	20	2	800
Telescope motion	50	2	5000
Subtotal	80		6400
Phase measurement errors	$\frac{175}{\sqrt{N}}$	$N/4$	7625
Total	118		14025
Time multiplier	6.2		

Figure 10 The diameter of the telescope needed to bootstrap a circular array of N telescopes. The maximum baseline (not the diameter of the circle) is 160 meters.
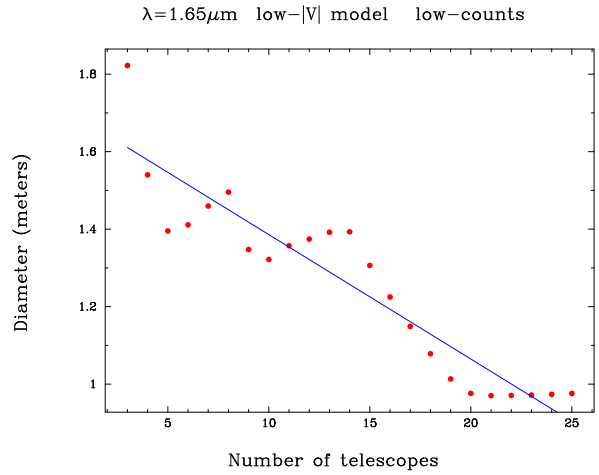

Figure 11 The diameter of the telescope needed to bootstrap a circular array of N telescopes assuming a system throughput a factor of three smaller than was used to produce Fig. 10 and Table 1.

The red dots in Fig. 10 show the results of the calculation. The scatter about the fitted curve is due to the structure in the low-visibility model and will almost certainly be different for every target.

Finally, we repeat the calculation assuming that the photometric throughput is three times smaller than our original assumptions. The result of that new calculation is shown in Figure 11.

6. DISCUSSION

From Fig. 10, we see that 1-meter telescopes should be sufficient. Those telescopes can be reduced to about 0.6 meters if we use a large number of them. For pessimistic throughput, Fig. 11, those diameters increase to 1.5m and 0.9m, respectively.

It is tempting to use this relationship between diameter and number of telescopes, N, to design a minimum-cost array. Before doing so, we must also consider how long it will take to form an image. The observation time is dominated by the time it takes to fill in the outer ring (all the azimuths for the maximum baseline length).

This is because the number of azimuths is proportional to the baseline length and the spectral bandpass per unique spatial frequency is inversely proportional to the baseline. Also, observation time is longer because $|V|$ decreases with increasing baseline length. The observing time will decrease linearly with N because with N telescopes, there are N longest baselines. We can also consider the second-longest baseline. For 5 telescopes, the second longest baseline is only 60% the length of the longest baseline and does not help. For 9 telescopes, that ratio increases to 88% and we can consider using the second-longest baseline to fill the outer ring. Unfortunately, the use of the second-longest baselines does not decrease the observing time because dividing photons between multiple baselines increases the time required for each baseline. The observing time required to form an image is inversely proportional to N.

However, using the second-longest baseline does decrease the imaging time which includes both the observing time and the overhead associated with moving the telescopes into the next configuration. Assuming we have the automation or manpower to move all the telescopes simultaneously, the time it takes to reconfigure the array should be roughly independent of the number of telescopes. For more than 15 telescopes, the number of baselines within 90% of the maximum length is $3N$. The best scenario is to do all the observing with a single configuration. With 23 telescopes, the fifth longest baseline is 80% of the longest baseline and a single configuration may be possible.

It is also important to remember the limitations of this calculation. The largest risk in this calculation is our assumption for how $|V|$ varies with baseline length and wavelength. The other risk is the interaction between the performance of the adaptive optics system and aperture averaging.

REFERENCES

[1] Schmitt, H., Mozurkewich, D., Jorgensen, A., Restaino, S., Armstrong, J., Baines, E., Hindsley, R. "Simulated Synthesis Imaging of Geostationary Satellites" *Proceedings of the AMOS conference, Wailea, Maui, Hawaii*, 2011

[2] Schmitt, H. R., Mozurkewich, D., Restaino, S. R., Armstrong, J. T., Baines, E. K., Hindsley, R. B., Jorgensen, A. M. "Simulated optical interferometric observations of geostationary satellites" *Proceedings of the SPIE* **8165**, 2011

[3] C Leinert, S. Bowyer, L. Haikala, M Hanner, M. Hauser, A.-C. Levasseur-Regourd, I. Mann, K. Mattila, W. Reach, W. Schlosser, H. Staude, G. Toller, J. Weiland, J. Weinbert, and A.Witt. "1977 referebce of diffuse night sky brightness", *Astron. and Astrophs, Suppl Ser.* **127**, pp. 1-99. 1998